RESEARCH ARTICLE

A cellphone-based colorimetric multi-channel sensor for water environmental monitoring

Yunpeng Xing[1,2,#], Boyuan Xue[2,#], Yongshu Lin[2], Xueqi Wu[2], Fang Fang[3], Peishi Qi (✉)[1],
Jinsong Guo (✉)[3], Xiaohong Zhou (✉)[2]

1 State Key Laboratory of Urban Water Resource and Environment, School of Environment, Harbin Institute of Technology, Harbin 150090, China
2 State Key Joint Laboratory of ESPC, Center for Sensor Technology of Environment and Health, School of Environment, Tsinghua University, Beijing 100084, China
3 Key Laboratory of the Three Gorges Reservoir Region's Eco-Environments of MOE, Chongqing University, Chongqing 400030, China

HIGHLIGHTS

- A cellphone-based colorimetric multi-channel sensor for in-field detection.
- A universal colorimetric detection platform in the absorbance range of 400–700 nm.
- Six-fold improvement of sensitivity by introducing a transmission grating.
- Quantifying multiple water quality indexes simultaneously with high stability.

GRAPHIC ABSTRACT
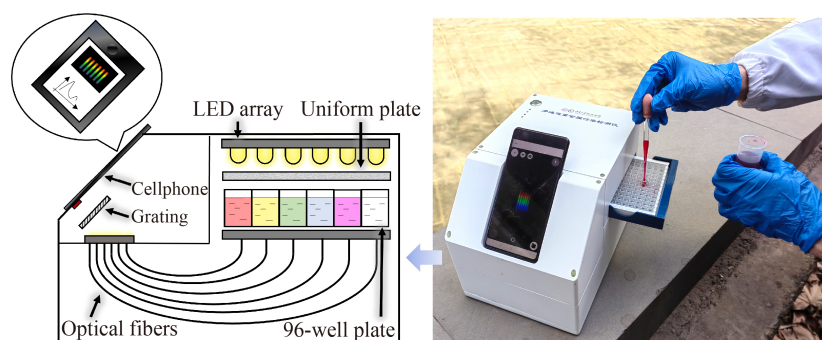
ABSTRACT

The development of colorimetric analysis technologies for the commercial cellphone platform has attracted great attention in environmental monitoring due to the low cost, high versatility, easy miniaturization, and widespread ownership of cellphones. This work demonstrates a cellphone-based colorimetric multi-channel sensor for quantifying multiple environmental contaminants simultaneously with high sensitivity and stability. To improve the sensitivity of the sensor, a delicate optical path system was created by using a diffraction grating to split six white beams transmitting through the multiple colored samples, which allows the cellphone CMOS camera to capture the diffracted light for image analysis. The proposed sensor is a universal colorimetric detection platform for a variety of environmental contaminants with the colorimetry assay in the range of 400–700 nm. By introducing the diffraction grating for splitting light, the sensitivity was improved by over six folds compared with a system that directly photographed transmitted light. As a successful proof-of-concept, the sensor was used to detect turbidity, orthophosphate, ammonia nitrogen and three heavy metals simultaneously with high sensitivity (turbidity: detection limit of 1.3 NTU, linear range of 5–400 NTU; ammonia nitrogen: 0.014 mg/L, 0.05–5 mg/L; orthophosphate: 0.028 mg/L, 0.1–10 mg/L; Cr (VI): 0.0069 mg/L, 0.01–0.5 mg/L; Fe: 0.025 mg/L, 0.1–2 mg/L; Zn: 0.032 mg/L, 0.05–2 mg/L) and reliability (relative standard deviations of six parallel measurements of 0.37%–1.60% and recoveries of 95.5%–106.0% in surface water). The miniature sensor demonstrated in-field sensing ability in environmental monitoring, which can be extended to point-of-care diagnosis and food safety control.

✉ Corresponding authors

E-mails: qipeishi@163.com (P. Qi); guo0768@cqu.edu.cn (J. Guo); xhzhou@mail.tsinghua.edu.cn (X. Zhou)

# These authors contributed equally to this work.

1 Introduction

Reliable colorimetric analysis technologies have been widely praised for their highly sensitive and selective responses towards various contaminants in environmental

monitoring (Zhai et al., 2013; Piriya et al., 2017; Priyadarshini and Pradhan, 2017). In principle, the chromogenic agent selectively reacts with the target in water samples, and the colored product reflects the specific absorbance spectrum. Obeying the Lambert-Beer law, the absorbance is proportional to the concentration of the absorbing species, providing the basis for the qualitative and quantitative detection of contaminants in water samples. The result of colorimetric assay can be observed by eye. However, this low-cost approach lacks accuracy. To replace the qualitative and semi-quantitative detection with a quantitative one, a photoelectron detector, such as a spectrophotometer (Lepot et al., 2016; Li and Hur, 2017) and a microplate reader (He et al., 2011; Fu et al., 2016) is required. However, this becomes expensive and thus difficult to be applied in resource-limited or remote environments (Mabey et al., 2004).

Giving consideration to both accuracy and cost, developing colorimetric analysis technologies on the commercial cellphone platform is gathering significant attention in environmental monitoring because of the low cost, high flexibility, easy to miniaturization, and widespread ownership of cellphone (Chen et al., 2014; Vashist et al., 2014; Capitán-Vallvey et al., 2015; Zhang and Liu, 2016; Kozitsina et al., 2018). Notably, the outstanding advantages of cellphone-based colorimetric technology is expected to greatly accelerate the environmental and health-related analysis capabilities in the remote or less-developed countries and regions (McCracken and Yoon, 2016; Andrachuk et al., 2019). As early as 2008, the first proof-of-concept cellphone-based colorimetric sensor was reported, which used a camera module of a cellphone to take a photograph and digitize the intensity of color associated with each colorimetric assay on the paper-based microfluidic chip (Martinez et al., 2008). To avoid the interference of light from the ambient environment, different integrated opto-mechanical attachments compatible with the built-in camera module of a cellphone were designed to digitally quantify the target concentration using colorimetric transmission assays that were implemented in disposable test tubes (Wei et al., 2014; Gao and Wu, 2016; Sajed et al., 2020; Xing et al., 2020). Due to its field-portability, inexpensive design, and wireless data connectivity, the detection platform was able to run on cellphones with high sensitivity and specificity, in addition to time and cost savings that could be helpful for distributed water contamination mapping as a function of both space and time (Liu et al., 2020). However, the majority of reported studies focused on single-channel colorimetric detection, which led to a limited detection efficiency, especially facing with complicated contaminants in water samples (Hong and Chang, 2014; Xing et al., 2020).

Research on cellphone-based multi-channel sensing systems has gained growing interest because the systems have the potential to simultaneously detect multiple targets in a single measurement, and the involved techniques for the rapid assessment of water samples are fast, robust and inexpensive (Wang et al., 2017a; Ma et al., 2021). To realize the multi-channel sensing capability, a mainstream technology pathway is to directly capture the colorimetric images from 96-well plates using a cellphone camera. Notably, a LED array with monochromatic light was generally used as the illumination source, and the transmitted light through each well was collected and transferred via 96 individual optical fibers (Berg et al., 2015). To avoid complex mechanical designs, a compact, smartphone-based, single-stripe colorimetric reader was designed, having a smaller size, lighter weight, and lower cost, hence more convenient for in-field applications (Wang et al., 2017b). More recently, external smartphone attachments were completely replaced with algorithms to interpret the videos from 96-well plates with colorimetric assays (Coleman et al., 2019). In all cases, the majority of strategies to improve the sensing capability of the cellphone-based system were based on a monochromatic light source, lacking universality and flexibility towards different contaminants which showed different absorption peaks.

Herein, we propose a cellphone-based colorimetric multi-channel sensor for water environmental monitoring. A white LED array was used as the incident light to illuminate a 96-well plate. The transmitted light from six wells was collected by six optical fibers and imaged by a cellphone camera after passing through a diffraction grating. The image was captured by a custom-designed cellphone app for analysis using a specific algorithm, yielding detection results which were displayed using the same app. The compact sensor was successfully tested for simultaneous detection of various environmental contaminants with an absorption wavelength range of 400–700 nm, achieving high sensitivity, specificity and reliability. The entire system exhibits high expansibility, which can be expanded to 96 channels by increasing the number of collecting optical fibers and the size of the grating.

2   Materials and methods

2.1   Design and fabrication of the cellphone-based multi-channel sensos

In order to establish a multi-channel sensing system with general detection capability in the whole visible light range and high sensitivity, the experimental setup demonstrating the light path design of the cellphone-based multi-channel sensor was shown in Fig. 1(A).

Notably, the overexposure caused by the strong power of LED light incident would always cause the return of the maximum signal value for the shooting of colored samples even at different concentrations. Conversely, the weak power of LED light would be associated with the weakened transmitted light, resulting in lower sensitivity
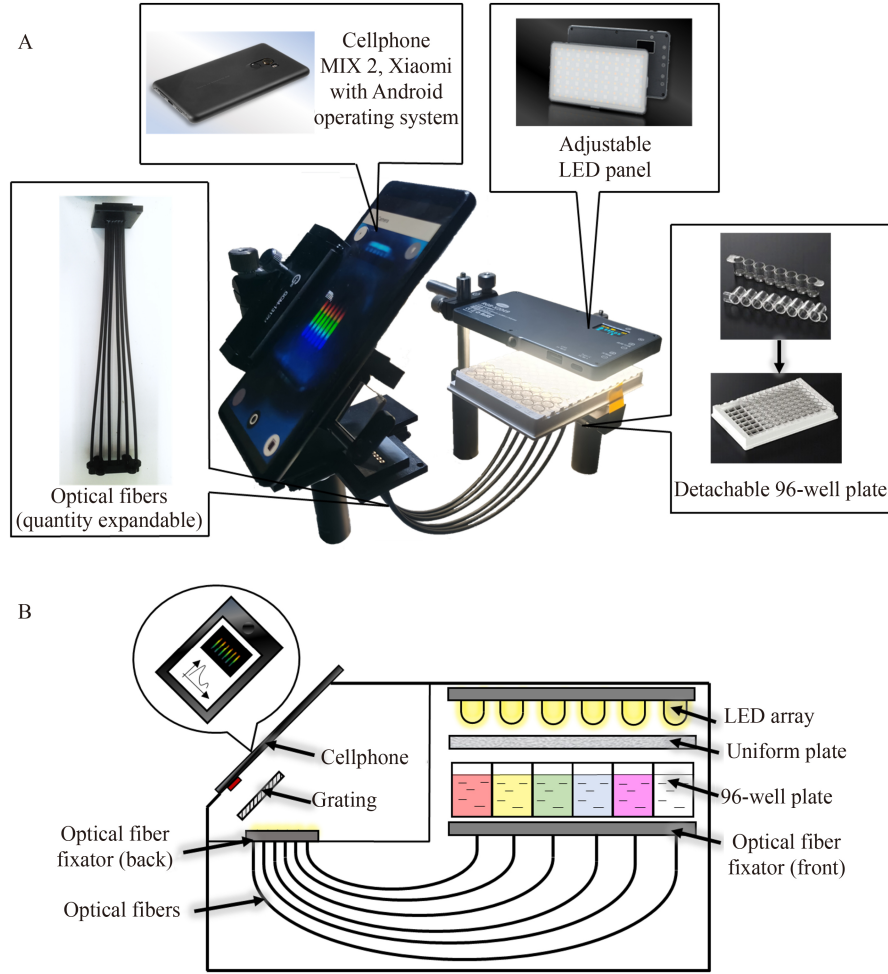
Fig. 1 Schematic diagram of the cellphone-based multi-channel sensor. (A) The light path design and the corresponding components of experimental setup, and (B) the structural design.

and limited response range. Therefore, an adjustable LED panel, accompanied with a specially designed direct current constant voltage to decrease the slight fluctuation of the power supply as similar as reported before (Xing et al., 2020), was utilized to optimize the power of luminance as high as possible, however without overexposure. After optimization (Fig. S1), the LED array with power of 0.5 W was selected for use. The light was homogenized through a double-side frosted uniform plate, and then entered into a transparent flat-bottom 96-well plate.

A commercialized transparent flat-bottom 96-well plate, which was supported by a 3D-printed plate holder, was used as the high-throughput colorimetric cuvette. Notably, if an 8 (hole/strip) × 12 (strip) detachable 96-well plate was adopted, it was suggested to use one strip instead of a whole plate to avoid waste under the condition of 6-channel application proposed in this work. The detachable plate also provided the flexible scalability to expand the channel numbers. The 3D-printed plate, as shown in Fig. S2, was designed with walls to avoid the interference of light path among channels. Moreover, a

black shading material, acrylonitrile butadiene styrene (ABS) plastic, was used for printing to isolate light scattering.

Plastic multi-mode optical fibers with core diameter of 2 mm, outer diameter of 3.5 mm and numerical aperture (NA) of 0.5 were selected to guide and converge the transmission light from different channels for imaging. Two optical fiber fixators were constructed and arranged at both ends of the fibers to ensure vertical incidence and exit of light (Fig. S3). Both ends of the fibers were polished to achieve fairly low surface roughness (Contour Arithmetic Mean Deviation of R_a 0.2 μm, ANSI/ASME B46.1-1988). The black plastic shells attached to the fiber cores were maintained to prevent stray light in the environment. The front ends of the fibers were placed under the bottom of the plate for 2.0 mm on the one hand to collect the light as much as possible and on the other hand to avoid the light interference from other channels. Compared with the image size of the transmitted light from the 96-well plate, this optical fiber imaging geometry shrunk approximately four times in a fairly compact space, significantly reducing the height of the

integrated sensor. Most importantly, the converged output fibers ensured the multi-channel light dispersion using only one grating. Meanwhile, because the optical fibers were used to receive light directly at the bottom of the 96-well plate, there was no need to add lens, apertures, and other complex optical components, which lessened the size of the integrated sensor and reduced the cost.

A ruling transmission grating with the size of 25 mm × 25 mm × 3 mm, the number of lines of 1200 lines/mm, the blazing angle of 36.9°, and the effective aperture of 0.9, fabricated by visible band B270 optical glass (Edmund Optics Co., Ltd, Shenzhen, China) with high surface finish (60/40, Scratch/Dig), was chosen to diffract the light (Note S1). In order to make the spectra of different channels uniform and clear, the distance and the angle between the output end of optical fibers and the transmission grating was set to 50 mm and 45°, the distance and the angle between the transmission grating and the CMOS camera of the cellphone was set to 30 mm and 0°. Under the above conditions, the first-order diffraction of transmission light was photographed with the CMOS camera of the cellphone.

A cellphone (MIX 2, Xiaomi, China) served as the image recognition and data processing unit. In the process of cellphone shooting, its CMOS camera photosensitivity (i.e. ISO), focus mode, focal length, color effect, exposure mode, and white balance were tested and determined. On the other hand, cellphone position, angle and other factors were optimized and fixed, in order to avoid the interference of these factors on the measurement.

After the optimization of the experimental setup, the cellphone-based multi-channel sensor structure was designed as shown in Fig. 1(B). More specifically, a planar white LED light array, i.e. a 96 bulb set with the power of 0.5 W (8 × 12, corresponding to 96-well plate), was used to improve the sensing sensitivity while failing caused by overexposure. The wavelength range of the white LED illumination was 400–700 nm, enabling the sensor capable of sensing contaminants in the whole visible light range. As a result, the apparent dimension of the integrated mechanical attachment to the cellphone was 16 cm in height and 26 cm × 18 cm in size (Fig. S4).

2.2 Image capture and analysis

The first-order diffraction spectrum of transmitted light was obtained through the dispersion of grating, and then the obtained images were analyzed to determine the image analysis model of this sensor based on Matlab2019b and Origin2021. Note S2 describes the Matlab codes in the process of image quantization.

As shown in Fig. 2(A), the parallel direction of spectral diffraction was defined as Y axis, and the vertical direction of spectral diffraction was defined as X axis. By introducing the monochromatic light lasers (Daheng Optics Co., Ltd, Beijing, China), the pixel corresponding to a specific wavelength was determined, and as a result the relationship between the Y direction position and the wavelength information was established (Vidal et al., 2021). Based on the above relationship, we firstly fixed the pixel position in the Y direction based on the specific absorption wavelength for different contaminant target, and then averaged the signal value along the X direction (Eq. 1).

$$\overline{SV} = \frac{1}{x_2 - x_1} \sum_{i=x_1}^{x_2} SV(i), \quad (1)$$

where $\overline{SV}$ is the average signal value at a specific wavelength, x_1 and x_2 are the edge pixel coordinates, i is the coordinate value between x_1 and x_2, and $SV(i)$ is the signal value at i pixel.

Common R (red), G (green), B (blue), H (hue), S (saturation), V (value), and gray value image analysis models were compared for optimization. Among them, R, G, and B models were obtained through RGB color model, and their values ranged from 0 to 255 (Long et al., 2014; Lin et al., 2016). H, S, and V models were separated through HSV color model, and their values ranged from 0 to 1 (after normalized process) (Cantrell et al., 2010). Gray model was a single variable value model transformed from RGB model and obtained by Eq. (2) (Vidal et al., 2021).

$$Gray = 0.299*R + 0.587*G + 0.114*B, \quad (2)$$

where $Gray$ is the gray value, R is the value of red channel, G is the value of green channel, and B is the value of blue channel.

Since turbidity has a scattering and absorbing effect on the full range of visible light, resulting in the overall reduction of transmission spectrum intensity, it is commonly used as a target to investigate the sensitivity and stability of the colorimetric sensor (Ceylan Koydemir et al., 2019). A series of turbidity standard solutions were prepared with formazin, and the signal values of different image analysis models were extracted at 680 nm (red region) to establish the calibration curve and hence compare their sensitivity, correlation, and detection range. For further verification, the targets, including ammonia nitrogen and orthophosphate, were tested. The optimal image analysis model was ultimately selected based on the above comparison.

Notably, the relationship of the signal values derived from the image analysis model and the target concentrations were obtained based on the Lambert-Beer law (Eq. (3)).

$$A = \log_{10}\frac{1}{T} = \log_{10}\frac{SV_0}{SV_i} = ac+b, \quad (3)$$

where A is the absorbance, T is the transmittance, SV_i and SV_0 are the average signal value at a specific wavelength with and without adding the chromogenic water sample (calculated by Eq. (1)), c is the concentration of the target, a and b is the slope and interrupt of the calibration curve, respectively.
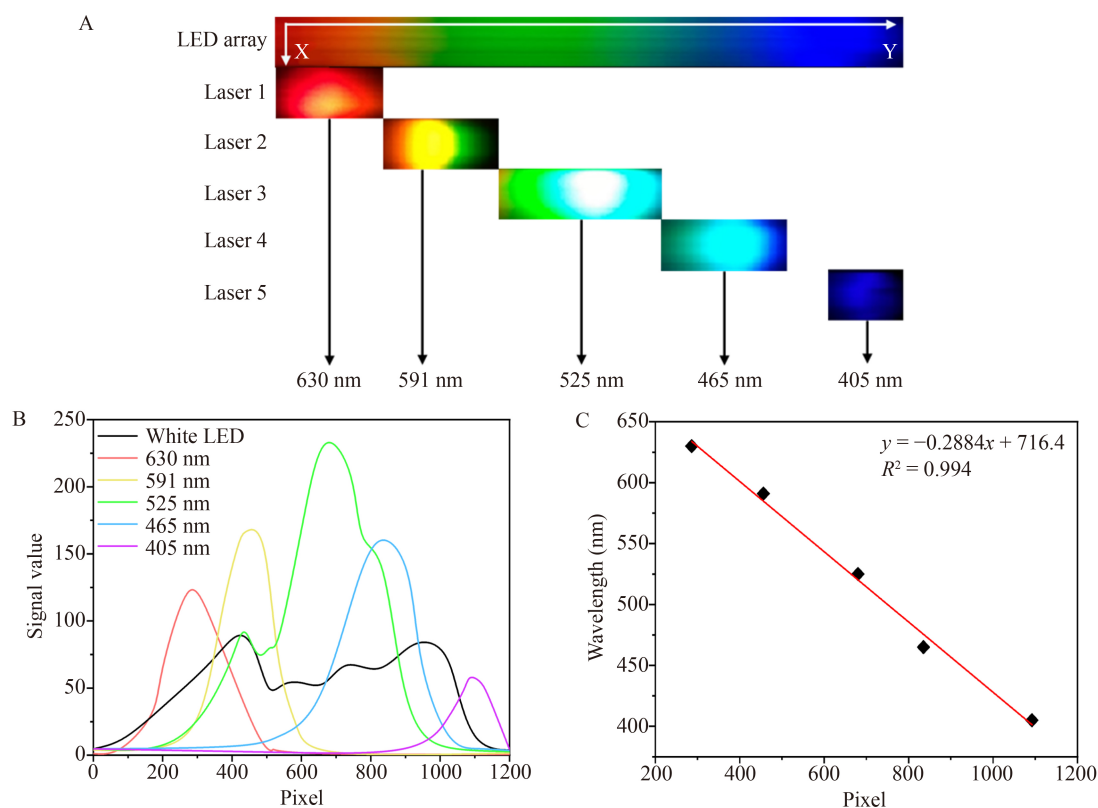
Fig. 2 Wavelength calibration for the cellphone-based multi-channel sensor. (A) Spectra of white LED and monochromatic light through the light dispersion of transmission grating; (B) Spectral curves of white LED and monochromatic light using the gray analysis model; (C) Linear fitting curve of wavelength and pixel.

2.3 Software design

A cellphone software named MyApp was designed to utilize the camera of the cellphone, project the image captured by the cellphone onto the two-dimensional canvas, and rotate it to a uniformly set angle to obtain the image. It captured the regions of interest (ROI), i.e. spectral image regions corresponding to different channels, which reduced the amount of calculation, optimized the running speed, and improved the accuracy of data in the subsequent calculation process compared with analyzing the whole image. The specific region parameters for further analysis were set in a configuration file (Note S3). Subsequently, MyApp converted the images obtained above into digital information to obtain the signal value from the optimal image analysis model. The mean value in the X direction was calculated to reduce the two-dimensional matrix of signals to one dimension (Eq. (1)), hence establishing the one-dimensional relationship between the signal value and the pixel. By establishing and storing the calibration curves for different contaminants set by users, MyApp calculated and directly outputted the concentrations. Moreover, the time and location of in-field testing were able to be recorded and stored in MyApp. When an image is captured, the regions of six channels (i.e. six spectra) can be analyzed at the same

time, and the results can be shown on the interface. Notably, the water quality index on each channel can be selected on MyApp. In this way, capturing one image can realize the detection of six water quality indexes simultaneously.

2.4 Performance evaluation for various environmental contaminants

Chemicals and colorimetric analytical methods used for various environmental contaminants in this study can be found in Note S4. As a proof-of-concept, each channel was set to detect one type of water quality indexes: channel 1 – turbidity, 2 – ammonia nitrogen, 3 – orthophosphate, 4 – Cr (VI), 5 – Fe, and 6 – Zn.

To verify the performance of this multi-channel sensor for environmental water matrices, the surface water was spiked with three levels of turbidity, ammonia nitrogen, orthophosphate, Cr (VI), Fe, and Zn. The water sample was taken from Hetang pond at Tsinghua campus (longitude 116°19′15.2″ E and latitude 40°0′5.9″ N). It is a landscape pond with area of about 1000 m^2. The results were compared with those measured by the commercial UV-visible spectrophotometer (HITACHI U-3900). Notably, the surface water was collected and then filtered with a 0.45 μm membrane filter to remove particulates

before the spiking and colorimetric sensing for six water quality indexes.

3   Results and discussion

3.1   Wavelength calibration

As revealed by Fig. 2(A), the light dispersion effect of the white LED through the transmission grating was of high quality with a relatively uniform distribution across the full spectrum. By using the monochromatic light lasers named laser 1 to 5 with the wavelength of 630 nm, 591 nm, 525 nm, 465 nm, and 405 nm, respectively, the spectrum of each monochromatic light was distributed on different pixels of the full spectrum of white LED, appearing typical band shapes, even though the spectra of monochromatic light lasers showed a certain spectral bandwidth. Taking the gray model as an example, the wavelength matching with the pixel was determined according to the position of the gray value peak (Fig. 2(B)). In our work, the monochromatic lights of 405 nm, 465 nm, 525 nm, 591 nm, and 630 nm were distributed at approximately 1092 pixels, 835 pixels, 680 pixels, 456 pixels, and 286 pixels, respectively. Thus, a linear fitting curve of wavelength and pixel were obtained with the curve equation of $y = -0.2884x + 716.4$, revealing that the resolution of this cellphone-based sensor was 0.2884 nm/pixel (Fig. 2(C)). The curve fitting showed a high linear correlation coefficient of 0.994, confirming that the transmission grating provided a good light dispersion effect.

3.2   Selection of image analysis models

Using turbidity as the target, a series of solutions with turbidity gradients were prepared to investigate the sensitivity of different image analysis models. The turbidity solution absorbed and scattered all wavelengths of light, therefore the transmitted image darkened as the turbidity increased (Fig. S5(A)). Correspondingly, significant decrease in the signal values was found in the red and blue regions associated with pixels of 0–380 and 800–930, respectively, when using model R, in the green region associated with pixels of 300–700 when using model G, and in the blue region associated with pixels of 550–750 when using model B (Fig. S5(B)–S5(D)). Notably, there was a concentration-independent upper limit of signal value (255) in the blue region of model B, leading to quantification impossible. Therefore, model B was not suitable for the detection of the target with the absorbance wavelength in the blue region. Similarly, with the increase of turbidity, significant increase in the signal values was found in the blue regions associated with pixels of 800–930 when using model S, and in the whole region associated with pixels of 0–1000 when using

model V; however, no significant change occurred in the spectral curve when using model H (Fig. S5(E)–S5(G)). Notably, just like model B, model V also showed a concentration-independent upper limit of signal value (255) in the blue region, indicating that it was very cautious to use the model V to interpret the signals of the target with the absorbance wavelength in the blue region. The gray value decreased with the increase of turbidity in the whole spectral region (Fig. S5(H)), indicating that the gray model was an ideal one to quantify the various targets with different absorbance wavelengths in the visible light range.

The signal value of each model was taken at the wavelength of 680 nm to determine the relationship between the turbidity concentration and the absorbance, resulting in the calibration curves based on Eq. (3). As depicted in Fig. 3(A), the sensitivities of the calibration curves derived from R, G, B, S, and V models were similar with the slopes in the range of 0.0010 to 0.0015. Except for S model, the linear correlation coefficients of models were greater than 0.99 (the highest 0.997 of model R), indicating that the R, G, B, and V models were highly correlated with the turbidity compared with the S model (Table 1). Even so, the slope of the calibration curve established by the gray model was 0.0016 (Fig. 3(B)), which was highest than the above models, and meanwhile the linear correlation coefficient reached 0.999 (Table 1). Similarly, by evaluating and comparing the calibration curves of ammonia nitrogen and orthophosphate derived from the R, G, B, S, V, and gray models (Figs. 3(C)–3(F)), the gray model showed highest sensitivities and most convincing linear correlation coefficients than other models (Table 1). Therefore, the gray model was selected for the subsequent experiments.

3.3   Android-based cellphone software development

To shoot clear and stable image, the parameters of cellphone CMOS camera were fixed as follows: ISO of 200, focus mode of FIXED, focal length of 10, color effect of NONE, exposure mode of LOCK, and white balance of LOCK. According to the Lambert-Beer law, the absorbance was proportional to the concentration of the colored substance when the thickness of the absorbent layer was fixed. And at a particular wavelength, the higher the absorbance of the sample, the darker the image taken by the cellphone. Accordingly, the signal value at a specific wavelength was calculated and converted into the absorbance by the built-in algorithm of the cellphone software, and the absorbance was used to establish calibration curves based on the concentration. The unknown samples were measured according to the established and stored calibration curves. Our current design of the sensor could analyze six water samples or six contaminants in one water sample simultaneously.

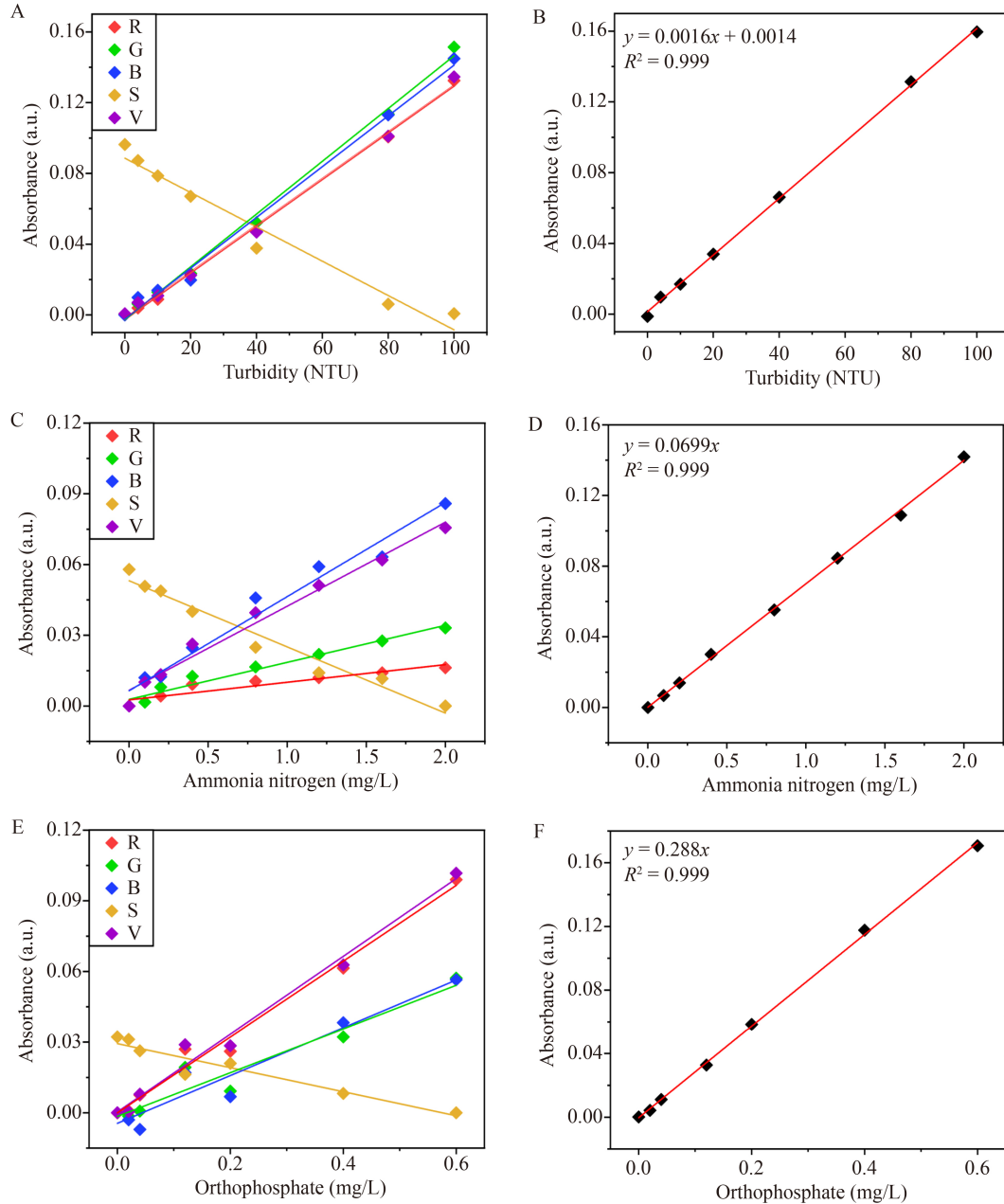It was worth mentioning that cellphone-based colorimetric

Fig. 3 Comparison of image analysis models for the cellphone-based multi-channel sensor. Calibration curves of (A) turbidity, (C) ammonia nitrogen, and (E) orthophosphate based on the R, G, B, S, and V models; and calibration curves of (B) turbidity, (D) ammonia nitrogen, and (F) orthophosphate based on the gray model.

multi-channel sensor was designed to meet the needs of rapid and in-field water quality analysis for users from governments, enterprises, and even families, most of whom are not professionally trained. As shown in Fig. 4, MyApp had an easy-to-use user interface to integrate the functions of calibration, image recognition, signal processing, real-time positioning, data storage, and data transmission. In the main menu of the software, users could create calibration curves, start new tests, view historical data, and change types and languages (Fig. 4(A)). For each contaminant, apart from the default standard curves

stored in the software, users had the option to create new standard curves according to their own preferences. After the selection or creation of the standard curve, a new test was initiated (Fig. 4(B)). In the shooting interface, the CMOS camera was started to shoot or upload an image file saved in the cellphone memory (Fig. 4(C)). After capturing the diffraction image of the samples, the intercepted region of the image was previewed and then used for the generation of signal value (gray value) curves of different channels on the screen before digital analysis (Fig. 4(D)). After pressing the "confirm" button,

Table 1 Slope, intercept, and correlation coefficient of calibration curves of turbidity, ammonia nitrogen, and orthophosphate based on different models

Substances	Factors	Model types						
		R	G	B	H	S	V	Gray
Turbidity	Slope	0.0013	0.0015	0.0014	−	−0.0009	0.0013	0.0016
	Intercept	−0.003	−0.003	-0.002	−	0.089	−0.002	0.0014
	Correlation coefficient	0.997	0.995	0.991	−	0.964	0.995	0.999
Ammonia nitrogen	Slope	0.007	0.016	0.040	−	−0.028	0.036	0.0070
	Intercept	0.003	0.003	0.006	−	0.053	0.007	1.4E−4
	Correlation coefficient	0.88	0.965	0.97	−	0.965	0.979	0.999
Orthophosphate	Slope	0.161	0.093	0.101	−	-0.051	0.165	0.288
	Intercept	−5.3E−5	0.002	−0.004	−	0.029	3.4E−4	−4.0E−4
	Correlation coefficient	0.985	0.934	0.930	−	0.919	0.985	0.999
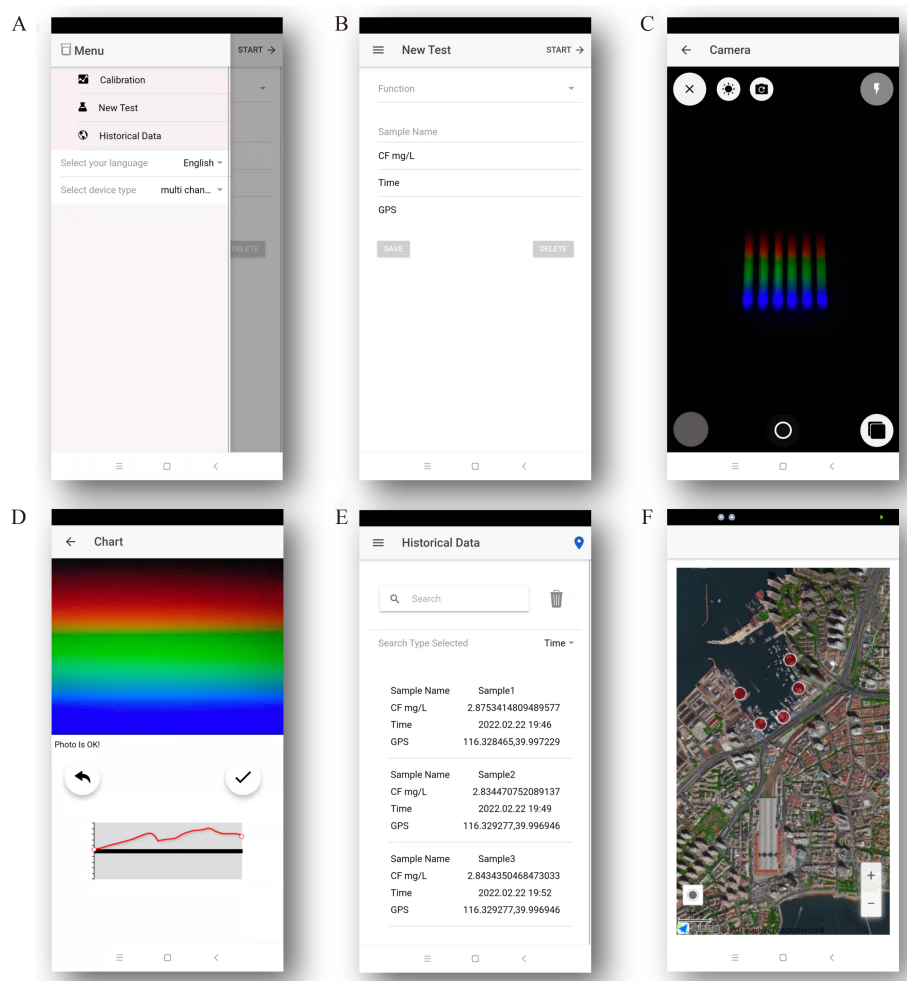
Fig. 4 Screen shots of the android-based cellphone software for water quality indexes analysis. (A) Main menu of the software; (B) Interface of creating a new test; (C) Interface of shooting or uploading an image; (D) Preview of the intercepted regions and signal value curves of different channels before generating the absorbance; (E) Interface of exhibiting historical data (including sample name, concentration, time, and GPS coordinates); (F) Interface of temporal and spatial analysis on the AutoNavi Map.

the absorbance of different channels at different wavelengths would be calculated automatically following Eq. (3), which was then converted into the concentration of the contaminants using the saved standard curves. Consequently, results were exhibited on the screen (Fig. 4(E)) with the test time and GPS coordinates saved in the

cellphone memory, which could be gathered to conduct temporal and spatial analysis, such as displaying on the AutoNavi Map (Fig. 4(F)).

Considering that the speed of image recognition and data processing were restricted by the hardware of the cellphone and the software design to a certain extent (Berg et al., 2015), we used a cloud server, Ubuntu Server 18.04 of Alibaba Cloud with 1 core, 4 GB memory (including virtual memory), and 10 GB hard disk, to proceed the image extraction, the data processing, and save the results for further management and analysis. It could greatly improve the detection speed, encrypt algorithms and data, support the massive data storage in real environmental monitoring, and hence possibly form a water quality big data network. The data transmission between the cellphone and the cloud server was realized by using mobile data or WLAN. It was worth mentioning that the sensor was able to run in the stand-alone version if there was no wireless network in the field. Normally, by transplanting the algorithm and operation to the powerful cloud server, it took no more than 10 seconds to proceed the whole analysis.

3.4   Detection performance of six water quality indexes simultaneously

As a proof-of-concept, six water quality indexes, including turbidity, ammonia nitrogen, orthophosphate, and three heavy metal ions of Cr (VI), Fe, and Zn, were tested simultaneously on the cellphone-based colorimetric six-channel sensor (Fig. 5). As expected, the absorbance, which was calculated by Eq. (3), increased with the increase of the concentrations of six water quality indexes. After fitting by least square method, the linear range of the multi-channel sensor was approximately 5–400 NTU for turbidity (Fig. 5(A)), 0.05–5 mg/L for ammonia nitrogen (Fig. 5(B)), 0.1–10 mg/L for orthophosphate (Fig. 5(C)), 0.01–0.5 mg/L for Cr (VI) (Fig. 5(D)), and 0.1–2 mg/L for Fe (Fig. 5(E)), and 0.05–2 mg/L for Zn (Fig. 5(F)), which met the requirement of Environmental quality standards for surface water of China (GB 3838-2002). According to the definition of the signal-to-noise ratio (S/N) = 3, the limits of detections (LODs) were calculated to be 1.3 NTU for turbidity, 0.014 mg/L for ammonia nitrogen, 0.028 mg/L for orthophosphate, 0.007 mg/L for Cr (VI), 0.025 mg/L for Fe, and 0.032 mg/L for Zn, respectively.

In theory, the diffraction grating can split the compound light into spectra with a high nm/pixel resolution. By diffraction, the cellphone camera can capture the imperceptible color change at a certain wavelength and decrease the interferences from light with other wavelengths, hence improving the sensor sensitivity. To confirm that, a direct imaging colorimetric sensing system was established and tested for comparison. As revealed by Fig. S6, the grating was not added and the light passed

through the 96-well plate, transmitted by optical fibers and then directly focused on the CMOS camera of the cellphone. Taking the turbidity as an example, the calibration curves obtained by using both systems was presented in Fig. S7. Obviously, when removing the grating, the linear range shrank from 5–400 NTU to 10–400 NTU, and the LOD increased from 1.3 NTU to 8.7 NTU. The results revealed that the introduction of the grating, especially after the delicate calculation and optimization, could significantly lift the sensitivity (slope increased 630.8%) and the fitting effect (R^2 increased 0.019), which was essential for the realization of accurate and stable detection.

Parallel tests ($n = 6$) were conducted by detecting the standard solutions of each water quality index with concentrations of 50% maximum detection range, which was used to evaluate the stability and repeatability of our multi-channel cellphone-based sensor. The relative standard deviations (RSD) of the absorbance measured at six times were in the range of 0.37% to1.60%, including 0.37% for turbidity, 1.60% for ammonia nitrogen, 1.34% for orthophosphate, 1.54% for Cr (VI), 1.12% for Fe, and 0.43% for Zn (Fig. 6). Results proved that the cellphone-based multi-channel sensor had excellent stability and repeatability.

3.5   Recovery of water quality indexes in surface waters

Ultimately, to confirm the capability of this technology to analyze different water quality indexes in environmental monitoring, the sensor was used to detect the spiked surface water taken from Tsinghua campus and results were demonstrated in Table 2 and compared with the conventional methods measured by the UV-Visible spectrophotometer. The spiked recoveries of six water quality indexes were in the range of 95.5% to 106.0%, proving the reliability of this technology. Besides, compared with the UV-Visible spectrophotometer results with the spiked recoveries in the range of 96.0% to 103.8%, the sensor technology showed slightly less stability in applications, however was more feasible, low-cost and simple-to-use, hence with great potential for in-field detection than other instrumental analysis technologies in lab.

4   Conclusions

In this study, a cellphone-based colorimetric multi-channel sensor was designed and demonstrated for in-field simultaneous detection of water quality indexes. In the sensor, the white light firstly went through the water samples in the 96-well plates, and was diffracted by the grating after the transmission of the optical fibers. Own to the diffraction grating, our sensor demonstrated an over six-fold improvement in sensitivity compared to the
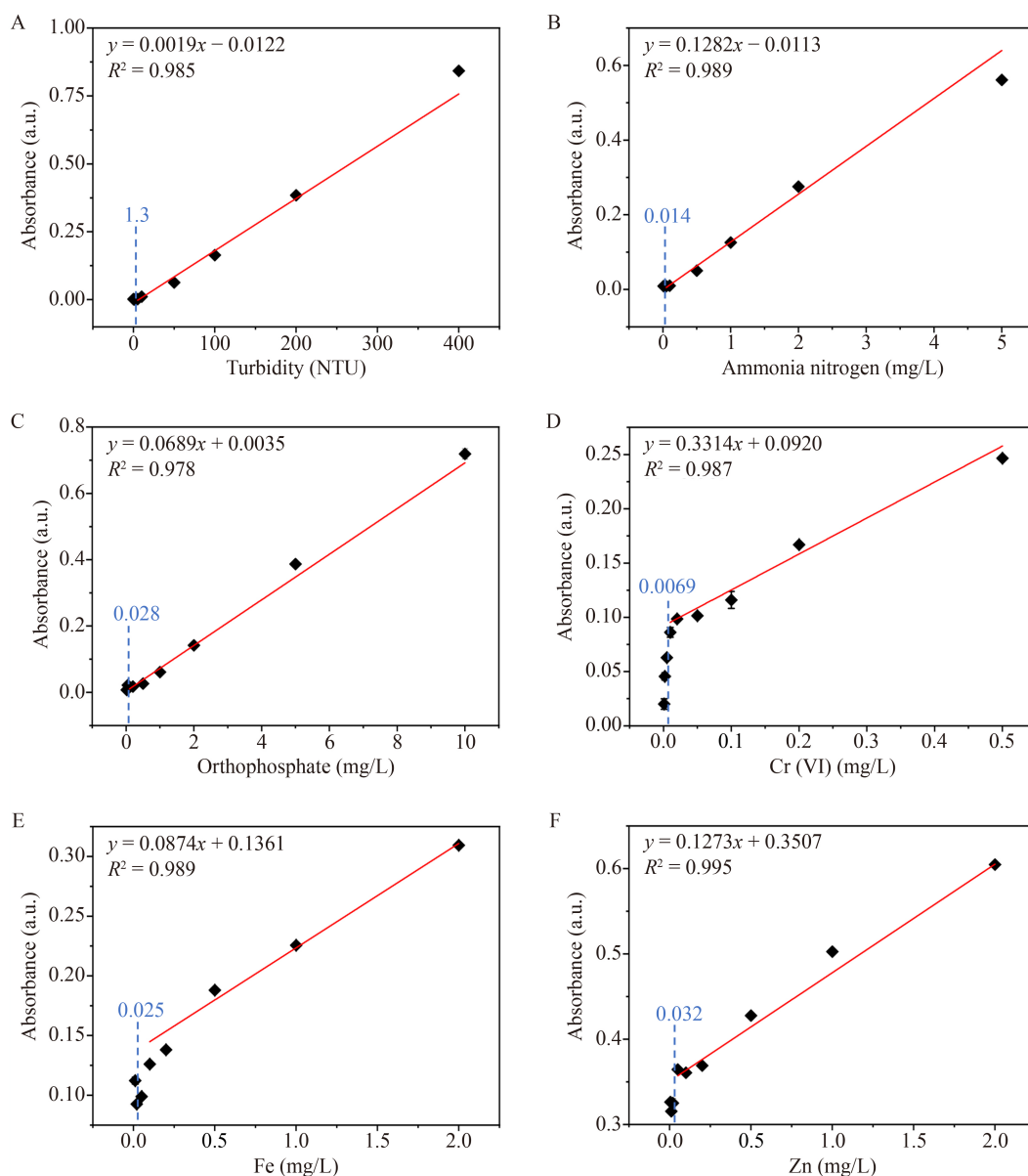
Fig. 5 Calibration curves of the multi-channel sensor (n = 3). Calibration curves for (A) turbidity, (B) ammonia nitrogen, (C) orthophosphate, and three heavy metal ions of (D) Cr (VI), (E) Fe, and (F) Zn. Blue words and dotted lines represent the LODs for different water quality indexes.

grating-less system. The postprocessing after the cellphone CMOS camera involves converting the gray value of the spectra into absorbance, in order to calculate the concentration according to the calibration curves. In our proof-of-concept demonstration, six indexes were successfully measured (turbidity: detection limit of 1.3 NTU, linear range of 5–400 NTU; ammonia nitrogen: 0.014 mg/L, 0.05–5 mg/L; orthophosphate: 0.028 mg/L, 0.1–10 mg/L; Cr (VI): 0.0069 mg/L, 0.01–0.5 mg/L; Fe: 0.025 mg/L, 0.1–2 mg/L; Zn: 0.032 mg/L, 0.05–2 mg/L). Moreover, high stability (RSD of 0.37%–1.60%) and excellent recoveries (95.5%–106.0%) demonstrated that our sensor is capable of conducting accurate detection in

real water matrices. Owing to the advantages of remarkable detection performance, low cost, easy operation, good portability, and multi-index measurement, our sensor is highly practical and important in the field of environmental monitoring, point-of-care diagnosis, food safety control, risk early warning, etc. Notably, by introducing the biorecognition materials, such as enzyme, antibody and functional nucleic acid, the sensor has the potential to be smarter to realize the detection of trace organic matters. Further, it can be expected that this technology would allow the detection channels up to 96 on the premise of overcoming the limitation of the volume or numbers of the diffraction grating.
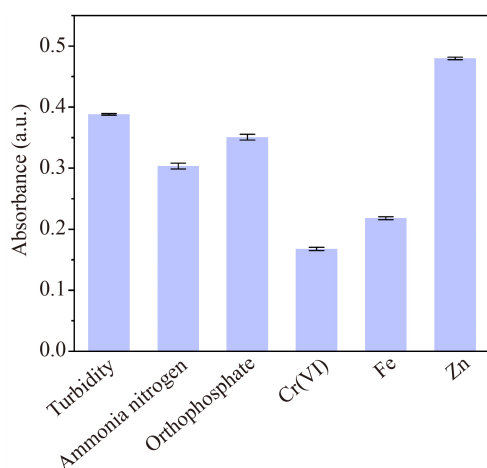
Fig. 6 Repeatability tests of our cellphone-based multi-channel sensor (n = 3). Concentrations of water quality indexes were set as follows: turbidity of 200 NTU, ammonia nitrogen of 2.5 mg/L, orthophosphate of 5 mg/L, Cr (VI) of 0.25 mg/L, Fe of 1 mg/L, and Zn of 1 mg/L.

Table 2 Recovery of six water quality indexes analysis in real water sample (n = 3 for our sensor)

Water quality index	Added (NTU for turbidity, mg/L for others)	Measured by spectrophotometer (NTU for turbidity, mg/L for others)	Measured by our sensor (NTU for turbidity, mg/L for others)	Recovery by our sensor (%)
Turbidity	0	3.3	4.3±0.8	−
	50	51.5	55.5±2.0	102.3±3.1
	100	106.5	108.4±2.0	104.1±2.1
	200	210.8	196.5±1.7	96.1±1.1
Ammonia nitrogen	0	0.055	0.048±0.008	−
	0.5	0.547	0.548±0.014	100.0±1.5
	1	1.067	1.094±0.023	104.6±2.2
	2	2.090	2.101±0.053	102.7±2.3
Orthophosphate	0	0.062	0.059±0.004	−
	1	1.054	1.061±0.013	100.2±1.6
	2	2.030	2.122±0.070	103.1±3.3
	4	4.011	3.881±0.046	95.5±1.1
Cr (VI)	0	0	< LOD	−
	0.05	0.048	0.052±0.001	105.6±1.8
	0.1	0.102	0.101±0.004	100.6±4.1
	0.2	0.201	0.196±0.004	98.1±1.9
Fe	0	0.053	0.061±0.012	−
	0.25	0.304	0.326±0.012	106.0±5.3
	0.5	0.564	0.561±0.010	99.9±2.0
	1	1.067	1.037±0.028	97.6±1.8
Zn	0	0.103	0.111±0.016	
	0.25	0.353	0.344±0.070	104.6±3.1
	0.5	0.604	0.609±0.071	105.2±5.5
	1	1.124	1.093±0.047	101.0±2.0

References

Andrachuk M, Marschke M, Hings C, Armitage D (2019). Smartphone technologies supporting community-based environmental monitoring and implementation: A systematic scoping review. Biological Conservation, 237: 430–442

Berg B, Cortazar B, Tseng D, Ozkan H, Feng S, Wei Q, Chan R Y L, Burbano J, Farooqui Q, Lewinski M, et al. (2015). Cellphone-Based Hand-Held Microplate Reader for Point-of-Care Testing of Enzyme-Linked Immunosorbent Assays. ACS Nano, 9(8): 7857–7866

Cantrell K, Erenas M M, de Orbe-Payá I, Capitán-Vallvey L F (2010). Use of the hue parameter of the hue, saturation, value color space as a quantitative analytical parameter for bitonal optical sensors. Analytical Chemistry, 82(2): 531–542

Capitán-Vallvey L F, López-Ruiz N, Martínez-Olmos A, Erenas M M, Palma A J (2015). Recent developments in computer vision-based analytical chemistry: A tutorial review. Analytica Chimica Acta, 899: 23–56

Ceylan Koydemir H, Rajpal S, Gumustekin E, Karinca D, Liang K, Göröcs Z, Tseng D, Ozcan A (2019). Smartphone-based turbidity reader. Scientific Reports, 9(1): 19901

Chen C Y, Chen Y H, Lin C F, Weng C J, Chien H C (2014). A review of ubiquitous mobile sensing based on smartphones. International Journal of Automation and Smart Technology, 4(1): 13–19

Coleman B, Coarsey C, Kabir M A, Asghar W (2019). Point-of-care colorimetric analysis through smartphone video. Sensors and Actuators. B, Chemical, 282: 225−231

Fu Q, Wu Z, Li X, Yao C, Yu S, Xiao W, Tang Y (2016). Novel versatile smart phone based Microplate readers for on-site diagnoses. Biosensors & Bioelectronics, 81: 524–531

Gao X, Wu N (2016). Smartphone-based sensors. Electrochemical Society Interface, 25(4): 79–81

He H, Tang B, Sun C, Yang S, Zheng W, Hua Z (2011). Preparation of hapten-specific monoclonal antibody for cadmium and its ELISA application to aqueous samples. Frontiers of Environmental Science & Engineering in China, 5(3): 409–416

Hong J I, Chang B Y (2014). Development of the smartphone-based colorimetry for multi-analyte sensing arrays. Lab on a Chip, 14(10): 1725–1732

Kozitsina A N, Svalova T S, Malysheva N N, Okhokhonin A V, Vidrevich M B, Brainina K Z (2018). Sensors based on bio and biomimetic receptors in medical diagnostic, environment, and food analysis. Biosensors (Basel), 8(2): 35

Lepot M, Torres A, Hofer T, Caradot N, Gruber G, Aubin J B, Bertrand-Krajewski J L (2016). Calibration of UV/Vis spectrophotometers: A review and comparison of different methods to estimate TSS and total and dissolved COD concentrations in sewers, WWTPs and rivers. Water Research, 101: 519–534

Li P, Hur J (2017). Utilization of UV-Vis spectroscopy and related data analyses for dissolved organic matter (DOM) studies: A review. Critical Reviews in Environmental Science and Technology, 47(3): 131–154

Lin T, Wu Y, Li Z, Song Z, Guo L, Fu F (2016). Visual monitoring of food spoilage based on hydrolysis-induced silver metallization of Au nanorods. Analytical Chemistry, 88(22): 11022–11027

Liu B, Zhuang J, Wei G (2020). Recent advances in the design of colorimetric sensors for environmental monitoring. Environmental Science. Nano, 7(8): 2195–2213

Long K D, Yu H, Cunningham B T (2014). Smartphone instrument for portable enzyme-linked immunosorbent assays. Biomedical Optics Express, 5(11): 3792–3806

Ma J, Du M, Wang C, Xie X, Wang H, Zhang Q (2021). Advances in airborne microorganisms detection using biosensors: A critical review. Frontiers of Environmental Science & Engineering, 15(3): 47

Mabey D, Peeling R W, Ustianowski A, Perkins M D (2004). Diagnostics for the developing world. Nature Reviews. Microbiology, 2(3): 231–240

Martinez A W, Phillips S T, Carrilho E, Thomas S W 3rd, Sindi H, Whitesides G M (2008). Simple telemedicine for developing regions: camera phones and paper-based microfluidic devices for real-time, off-site diagnosis. Analytical Chemistry, 80(10): 3699–3707

McCracken K E, Yoon J Y (2016). Recent approaches for optical smartphone sensing in resource-limited settings: A brief review. Analytical Methods, 8(36): 6591–6601

Piriya V S A, Joseph P, Daniel S C G K, Lakshmanan S, Kinoshita T, Muthusamy S (2017). Colorimetric sensors for rapid detection of various analytes. Materials Science & Engineering. C, Materials for biological applications, 78: 1231−1245

Priyadarshini E, Pradhan N (2017). Gold nanoparticles as efficient sensors in colorimetric detection of toxic metal ions: A review.

Sensors and Actuators. B, Chemical, 238: 888−902

Sajed S, Kolahdouz M, Sadeghi M A, Razavi S F (2020). High-performance estimation of lead ion concentration using smartphone-based colorimetric analysis and a machine learning approach. ACS Omega, 5(42): 27675–27684

Vashist S K, Mudanyali O, Schneider E M, Zengerle R, Ozcan A (2014). Cellphone-based devices for bioanalytical sciences. Analytical and Bioanalytical Chemistry, 406(14): 3263–3277

Vidal E, Lorenzetti A S, Garcia C D, Domini C E (2021). Use of universal 3D-printed smartphone spectrophotometer to develop a time-based analysis for hypochlorite. Analytica Chimica Acta, 1151: 338249

Wang L J, Chang Y C, Sun R, Li L (2017a). A multichannel smartphone optical biosensor for high-throughput point-of-care diagnostics. Biosensors & Bioelectronics, 87: 686–692

Wang Y, Zeinhom M M A, Yang M, Sun R, Wang S, Smith J N, Timchalk C, Li L, Lin Y, Du D (2017b). A 3D-printed, portable, optical-sensing platform for smartphones capable of detecting the herbicide 2,4-dichlorophenoxyacetic acid. Analytical Chemistry, 89(17): 9339–9346

Wei Q, Nagi R, Sadeghi K, Feng S, Yan E, Ki S J, Caire R, Tseng D, Ozcan A. Detection and spatial mapping of mercury contamination in water samples using a smart-phone. ACS Nano, 2014, 8(2): 1121−1129

Xing Y, Zhu Q, Zhou X, Qi P. A dual-functional smartphone-based sensor for colorimetric and chemiluminescent detection: A case study for fluoride concentration mapping. Sensors and Actuators. B, Chemical, 2020, 319: 128254

Zhai J, Yong D, Li J, Dong S. A novel colorimetric biosensor for monitoring and detecting acute toxicity in water. Analyst, 2013, 138(2): 702−707

Zhang D, Liu Q. Biosensors and bioelectronics on smartphone for portable biochemical detection. Biosensors & Bioelectronics, 2016, 75: 273−284